

Magnetization-Induced Band Shift in Ferromagnetic Weyl Semimetal $\text{Co}_3\text{Sn}_2\text{S}_2$ Run Yang^{1,2,*}, Tan Zhang^{1,2,*}, Liqin Zhou^{1,2}, Yaomin Dai,³ Zhiyu Liao,^{1,2}
Hongming Weng,^{1,2,4,5,†} and Xianggang Qiu^{1,2,4,‡}¹*Beijing National Laboratory for Condensed Matter Physics, Institute of Physics, Chinese Academy of Sciences, Beijing 100190, China*²*School of Physical Sciences, University of Chinese Academy of Sciences, Beijing 100049, China*³*Center for Superconducting Physics and Materials, National Laboratory of Solid State Microstructures and Department of Physics, Nanjing University, Nanjing 210093, China*⁴*Songshan Lake Materials Laboratory, Dongguan, Guangdong 523808, China*⁵*CAS Center for Excellence in Topological Quantum Computation, Beijing 100190, China*

(Received 19 October 2019; accepted 4 February 2020; published 21 February 2020)

The discovery of magnetic Weyl semimetal (magnetic WSM) in $\text{Co}_3\text{Sn}_2\text{S}_2$ has triggered great interest for abundant fascinating phenomena induced by band topology conspiring with the magnetism. Understanding how the magnetization affects the band structure can give us a deeper comprehension of the magnetic WSMs and guide us for the innovation in applications. Here, we systematically study the temperature-dependent optical spectra of ferromagnetic WSM $\text{Co}_3\text{Sn}_2\text{S}_2$ experimentally and simulated by first-principles calculations. Our results indicate that the many-body correlation effect due to Co $3d$ electrons leads to the renormalization of electronic kinetic energy by a factor about 0.43, which is moderate, and the description within density functional theory is suitable. As the temperature drops down, the magnetic phase transition happens, and the magnetization drives the band shift through exchange splitting. The optical spectra can well detect these changes, including the transitions sensitive and insensitive to the magnetization, and those from the bands around the Weyl nodes. The results support that, in magnetic WSM $\text{Co}_3\text{Sn}_2\text{S}_2$, the bands that contain Weyl nodes can be tuned by magnetization with temperature change.

DOI: [10.1103/PhysRevLett.124.077403](https://doi.org/10.1103/PhysRevLett.124.077403)

Recently, the shandite compound $\text{Co}_3\text{Sn}_2\text{S}_2$ has attracted lots of attention since it not only shows intrinsic ferromagnetism but also is proposed to have three pairs of Weyl points around the Fermi level in the first Brillouin zone [1–5]. For its quasi-two-dimensional crystal structure, low carrier density, and strong anomalous Hall effect, $\text{Co}_3\text{Sn}_2\text{S}_2$ has been thought as a potential candidate to realize the quantum anomalous Hall effect [6,7] in its two-dimensional (2D) limit [1,8,9]. As a magnetic Weyl semimetal (WSM) [10], the magnetic ordering states are expected to have interactions with Weyl nodes [2,3], so that the topological properties from WSM can be finely tuned through control of magnetization [2,11]. It has been found that upon cooling, the magnetization and anomalous Hall conductivity (AHC) of $\text{Co}_3\text{Sn}_2\text{S}_2$ vary accordingly [1,2], and the first-principles calculations of AHC at different magnetization has shown their intrinsic relationship through the changes in the position of Weyl nodes [2]. However, there still lacks a thorough comprehension of the magnetization-dependent properties in magnetic WSMs. Since the band structure dominates the electronic properties, it is imperative to know how the magnetization affects their band topology.

Because of large penetration depths, optical spectroscopy is more sensitive to bulk properties. Comparing with the AHC measurements, the advantages of optical spectra

measurement are as follows. First, the optical spectrum is sensitive to both occupied and unoccupied bands, which constitute the Weyl nodes in WSM. In contrast, AHC is only sensitive to the one crossing Fermi level [7,12–16]. Second, on considering optical selection rule and peak position, one can definitely identify the contributions from Weyl nodes [17–19]. Moreover, transport measurement like AHC requires high techniques and high quality of the whole device [14]. The extrinsic factors make the understanding of the intrinsic mechanisms very difficult.

In this Letter, combining optical spectroscopy and first-principles calculations, we systematically investigate the band structure of $\text{Co}_3\text{Sn}_2\text{S}_2$ at various temperatures (T s) above and below its Curie temperature [$T_C \sim 177$ K, Fig. 1(b)]. We have clearly demonstrated how the band structure evolves and identified both the magnetization sensitive and nonsensitive contributions to different optical conductivity peaks. The contributions around the Weyl nodes are also identified. Furthermore, we have found that the electron-electron correlation effect in this magnetic compound is not strong, and the electronic kinetic energy renormalization factor is around 0.43. The first-principles calculations within local density functional approximation are suitable. These give out strong supports that, in $\text{Co}_3\text{Sn}_2\text{S}_2$, the bands that contain Weyl points can be tuned by magnetization.

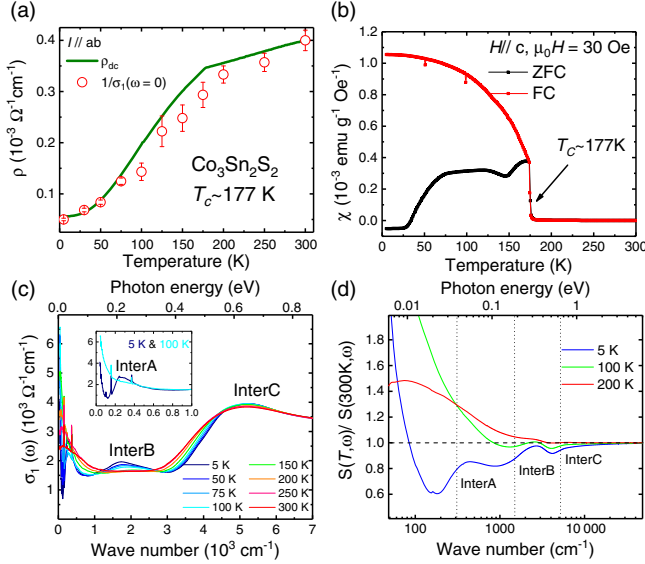


FIG. 1. (a) The dc resistivity (ρ) of $\text{Co}_3\text{Sn}_2\text{S}_2$ (solid line) with the zero-frequency values of optical conductivities (red circles). (b) The T dependence of magnetic susceptibility $\chi(T)$ with a zero-field-cooling and field-cooling mode at $\mu_0 H = 30$ Oe for $H \parallel c$. The black arrow denotes the Curie Weiss temperature $T_C \sim 177$ K. (c) The T -dependent optical conductivity $\sigma_1(\omega)$ from 30 to 7000 cm^{-1} . Inset shows the optical conductivity at 5 and 100 K in the far-infrared range. Three interband absorption peaks from low to high energy are denoted by “InterA,” “InterB,” and “InterC,” respectively. (d) The ratio of the integrated spectral weight $S(T, \omega)/S(300 \text{K}, \omega)$ as a function of cutoff frequency (ω) at different temperatures. $S(T, \omega) = (Z_0/\pi^2) \int_0^\omega \sigma_1(\omega', T) d\omega'$, in which $Z_0 = 377 \Omega^{-1}$ is the vacuum impedance.

The T dependence of the real part of the in-plane optical conductivity [$\sigma_1(\omega)$] is shown in the energy range from 20 cm^{-1} (2.5 meV) to 7000 cm^{-1} (0.87 eV) [Fig. 1(c), see details of the measurements in the Supplemental Material [20]]. The conductivities at 100 (blue) and 5 K (black) are shown in the infrared region for comparison [inset of Fig. 1(c)]. At first glance, they consist of a Drude peak at zero-frequency and several other Lorentz peaks at finite frequencies. Besides, several sharp features in conductivities are observed at 155, 245, and 370 cm^{-1} , which originate from the infrared-active phonons. Based on the Kubo function, $\sigma_1(\omega)$ is proportional to the joint density of states, the peak at zero frequency (Drude) represents the intraband response, and the one at a finite frequency (Lorentz) comes from the interband transitions [32]. The extrapolated values for the dc conductivity [$\sigma_1(\omega \rightarrow 0) \equiv \sigma_{\text{dc}}$] [circles in Fig. 1(a)] are virtually identical to the resistivity, indicating excellent agreement between optical and transport measurements. Upon cooling, $\sigma_1(\omega)$ shows apparent T dependence, especially in the mid-infrared range, indicating that the band structure varies prominently with decreasing T .

At room temperature (300 K), the optical conductivity shows a typical metallic character, with a Drude-like free-carrier response at low frequencies. Besides a Lorentz-like

feature centered around 5000 cm^{-1} and some phonon peaks, in the range from 1000 to 3000 cm^{-1} the optical conductivity is almost frequency independent. This plateau persists down to $T_C \sim 177$ K, below which it gradually evolves into a Lorentzian, which grows up and moves to lower energy range with decreasing T . Meanwhile, the peak centered at 5000 cm^{-1} starts to strengthen and moves to higher energy. These features indicate that, in the FM state, the band structure changes dramatically with T . The Drude peak at zero frequency narrows continuously with decreasing T , implying suppressed quasiparticle scattering. Below 100 K, the intraband response is greatly suppressed, evolving into two components: an ultrasharp Drude peak and a new interband absorption peak at 310 cm^{-1} [inset of Fig. 1(c)]. In the corresponding reflectivity (Fig. S1 in the Supplemental Material [20]), a sharp plasma edge emerges below 100 K, indicating much coherent quasiparticle response [33,34].

From the spectral weight of $\sigma_1(\omega)$ [Fig. 1(d)], we see that, from 300 to 200 K, the $S(T, \omega)$ is gradually transferred from high to low energy range, indicating an enhanced intraband response [35]. While, below $T_C \sim 177$ K, spectral weight below 1000 cm^{-1} is transferred back to high energy range, accumulating in peaks at 2000 (InterB) and 5000 cm^{-1} (InterC), respectively. However, below 100 K, the spectral weight of low-energy intraband response is greatly suppressed, giving rise to a new absorption peak around 310 cm^{-1} [38 meV, interA in the inset of Fig. 1(c)]. Although such behavior is similar to the spin or charge-density-wave transition [36,37], during which a gap emerges on the Fermi surface, in $\text{Co}_3\text{Sn}_2\text{S}_2$, no phase transition was predicted and observed in previous studies [1,2].

To get some more quantitative estimates of parameters determining the optical response, we fit the optical conductivity using a Drude-Lorentz model with the dielectric function $\tilde{\epsilon} = \epsilon_1 + i\epsilon_2$ [32,38]

$$\epsilon(\omega) = \epsilon_\infty - \sum_i \frac{\omega_{p,D;i}^2}{\omega^2 + \frac{i\omega}{\tau_{D,i}}} + \sum_j \frac{\Omega_j^2}{\omega_j^2 - \omega^2 - i\omega\gamma_j}, \quad (1)$$

where ϵ_∞ is the real part at high frequency. In the first sum $\omega_{p,D;i}^2 = 4\pi n_i e^2 / m_i^*$ and $1/\tau_{D,i}$ are the square of plasma frequency and scattering rate for the delocalized (Drude) carriers, respectively, and n_i and m_i^* are the carrier concentration and effective mass. In the second summation, ω_j , γ_j , and Ω_j are the position, width, and strength of the j th vibration or bound excitation. The complex conductivity is $\tilde{\sigma}(\omega) = \sigma_1 + i\sigma_2 = -2\pi i\omega[\tilde{\epsilon}(\omega) - \epsilon_\infty]/Z_0$ ($Z_0 \simeq 377 \Omega$ is the impedance of free space), and the real part $\sigma_1(\omega)$ is fitted using a nonlinear least-squares technique.

The fit to the data at 100 K shown in Fig. 2(a) indicates that the optical conductivity can be reproduced quite well using one Drude peak and three Lorentz oscillators at 310, 1600, and 5100 cm^{-1} ($\simeq 38, 198, \text{ and } 632$ meV). Below

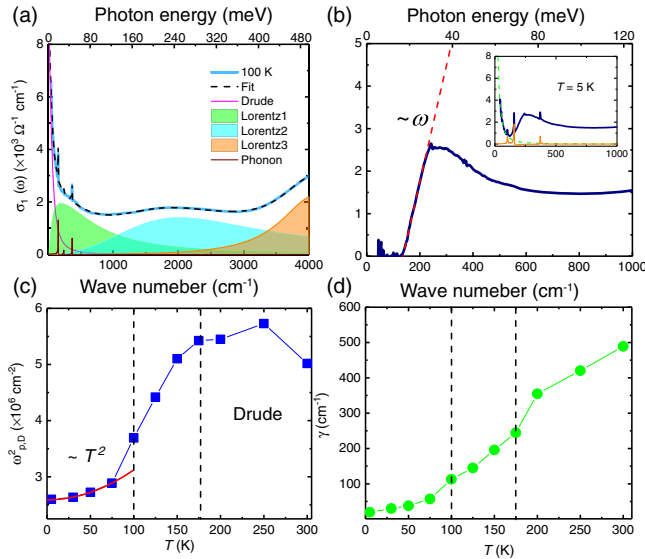


FIG. 2. (a) The Drude-Lorentz fit to the complex optical conductivity of $\text{Co}_3\text{Sn}_2\text{S}_2$ at 100 K. (b) The optical conductivity at 5 K, after the Drude peak and phonon peaks below 300 cm^{-1} have been subtracted. Inset: the whole optical conductivity at 5 K, the green dashed line represents the intraband response (Drude), origin line is the fit to the phonon modes below 300 cm^{-1} (with a series of Lorentz peaks). (c) and (d) are the fitted value for the square of plasma frequency ($\omega_{p,D}^2$) and the scattering rate (γ) of Drude component, the red line in (c) is the T^2 fit to the square of plasma frequency. The dashed lines in (c) and (d) denotes the Curie temperature ($T_C \sim 177 \text{ K}$) and 100 K.

100 K, Drude response is suppressed dramatically, revealing the absorption peak centered at 310 cm^{-1} [inset of Fig. 1(c)]. We realize that it is hard to describe this peak with a simple Lorentz peak for its steep edge on the low-energy side. To investigate this low-energy interband transition, in Fig. 2(b), we have subtracted the Drude response and sharp phonon peaks [inset of Fig. 2(b)] [39]. In the residual conductivity, which purely comes from interband transitions, an unusual feature is a ω -linear conductivity from 130 to 230 cm^{-1} (16–29 meV), which indicates the presence of 3D linear bands near the Fermi level [17,19,39,40] (see more discussion in the Supplemental Material [20]).

The T dependence of the square of plasma frequency ($\omega_{p,D}^2$), i.e., the Drude weight, and the scattering rate ($1/\tau_D$) of Drude response are shown in Figs. 2(c) and 2(d), respectively. As the temperature is reduced, the Drude weight is first enhanced a little at 200 K and then suppressed after the FM transition. Below 100 K, $\omega_{p,D}^2$ is considerably suppressed and shows T^2 dependence, which agrees well with theoretical predictions for Weyl semimetals [41]. The $1/\tau_D$ decreases dramatically with the T , from 495 cm^{-1} at 300 K to 15 cm^{-1} at 5 K. Here, we notice that even though previous investigations on $\text{Co}_3\text{Sn}_2\text{S}_2$ predict the emergence of Weyl points right below $T_C \sim 177 \text{ K}$ [3], we only

observed the distinct signature of linear bands at $T < 100 \text{ K}$. The optical response indicates that, above 100 K, the response from other parabolic bands may superimpose over the response from the bands with linear dispersion. Below 100 K, the parabolic bands may gradually move away from Fermi level, resulting in a Lifshitz transition, which leaves the linear bands dominating the low-energy response. At 5 K, both the steep plasma edge in reflectivity (Fig. S1 in the Supplemental Material [20]) and the ultranarrow Drude peak in optical conductivity reflect the coherence of the linear bands [17,18].

To better understand the optical conductivity as well as the electronic properties, we have simulated the band structure and optical conductivity of $\text{Co}_3\text{Sn}_2\text{S}_2$ through the first-principles calculations. Because of the weaker magnetic fluctuations as T drops, the effective moment on Co atoms increases upon cooling. To mimic the T effect, the magnetic moment on Co is constrained at different values during the self-consistent calculation. In the paramagnetic (PM) state, the calculated band structure shows a semi-metallic feature in Fig. 3(a). Without including SOC, there exist two linear band crossings marked in dashed circles in $U-L$ and $L-\Gamma$ paths as protected by the mirror symmetry. These crossing points are on the nodal rings in the mirror planes [2]. On considering SOC, the band gap opens along the rings. Figures 3(b) and 3(c) are band structures calculated with the magnetic moments of Co atoms constrained at 0.15 and $0.33 \mu_B$, respectively. The latter one is in the ground state without any constraint. The spin exchange splitting gradually separates the bands into spin up and spin down channels. The spin-up one shifts closer to the Fermi level, and the spin-down moves to higher energy. In the case without SOC (Fig. S5), the nodal rings protected by the mirror plane are kept well in both channels. The Fermi surfaces in PM and FM are different, as shown in Figs. 3(d) and 3(e). It becomes a half-metal in the ground state (Fig. S5b in the Supplemental Material [20]). When SOC is further considered, the crossing points open gaps along the nodal rings, and away from the mirror planes, three pairs of Weyl points appear. The band structure around Weyl point is described in Fig. S2 in the Supplemental Material [20] and Refs. [1–3].

Next, we calculated the optical conductivity with different magnetization. In addition to the interband contributions, the intraband transition is included as the Drude model. The plasma frequency ω_p contributed to the Drude peak can be obtained from band structure calculations. It is obtained as 1.73 eV for PM, and 1.34 and 0.94 eV for FM with the magnetic moments of 0.15 and $0.33 \mu_B$ on Co atoms, respectively. ω_p decreases with magnetization, which is consistent with the shrinking of Fermi surfaces in Figs. 3(d) and 3(e), as well as the decreasing of carrier density [1]. The scattering rate $1/\tau_D$ is parametrized as 0.17 , 0.05 , and 0.03 eV to mimic the decreasing (increasing) of T (lifetime) and to well fit the experimental spectra.

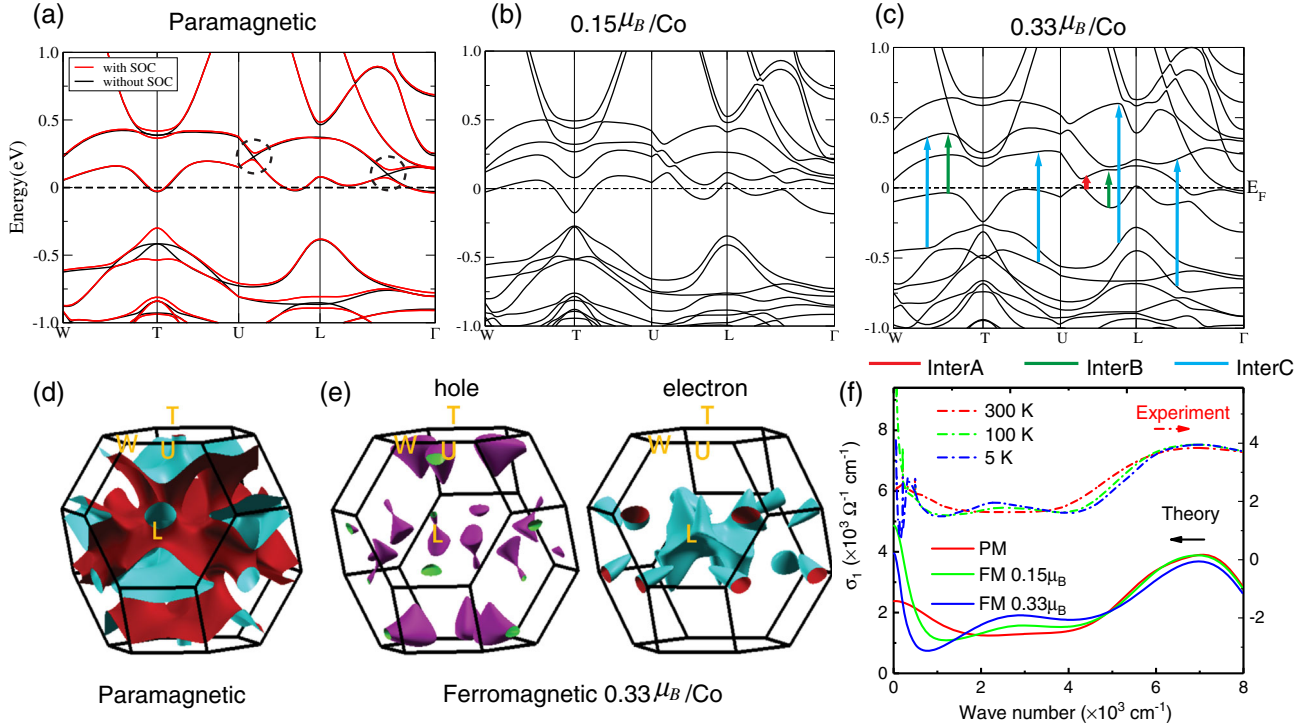


FIG. 3. (a) The band structure along high-symmetry paths with (red) and without (black) spin-orbital coupling (SOC). The dashed circles denote the band crossing opened by SOC. (b) and (c) show the band [0.15 μ_B /Co (b), 0.33 μ_B /Co (c)]. Comparing with the measured optical conductivity, we ascribe the three absorption peaks in Fig. 1(c) to interband transitions “InterA,” “InterB,” and “InterC,” respectively. The band structures in (b) and (c) are calculated with SOC. (d) and (e) are Fermi surfaces in paramagnetic (PM) and ferromagnetic (FM, 0.33 μ_B /Co) state. (f) displays the simulated optical conductivities (solid lines) based on band structure calculation (with SOC) in the PM and FM (0.15 μ_B /Co and 0.33 μ_B /Co) states in comparison with experimental results (dashed dot lines). In the experimental plot, the wave number is scaled by a factor 1.33 to well match the theoretical one, where the band renormalization effect is not considered.

Within these settings, the theoretical spectra are shown in Fig. 3(f) together with the experimental ones. It is noted that the experimental spectra are replotted with the incident photon wave number being scaled by a factor of 1.33 to match the InterC in Fig. 1(c) with the calculated position [42]. This difference between the experimental and theoretical results comes from the correlation effect due to 3d orbitals of Co, which is not considered during the calculation within local density approximation. To further estimate the correlation strength, the renormalization of the electronic kinetic energy is estimated by comparing the spectral weight of the intraband response in measured (5 K) and simulated (0.33 μ_B /Co) optical conductivity [43]. The renormalization factor 0.43 corresponds to a moderate electron correlation (see more detail in the Supplemental Material [20]). However, the qualitative consistency between the calculated and scaled experimental spectra indicates that the single-particle approximation can catch the most essential features of this material.

One can also notice that the optical conductivity around InterC is not sensitive to the magnetization or spin splitting in bands, while InterB is very sensitive and appears after the magnetic phase transition. Considering the optical selection

rule, including interband transitions energy, the enhanced joint density of states from roughly parallel bands and the angular momentum change without spin flipping, we find a lot of interband transitions that contribute to InterC [Fig. S7(c) in the Supplemental Material]. After considering the contribution to InterC, in Fig. 3(c), we use blue arrows to denote the dominant ones (see more detail in the Supplemental Material [20]). The associated occupied and unoccupied bands are from Co 3d t_{2g} and e_g orbitals, respectively. These bands are separated due to octahedral crystal-field splitting being irrelevant to the spin-exchange splitting. For the InterB, after considering all the possible interband transitions around 3000 cm^{-1} (0.37 eV), we mark the interband contributions by green arrows, and they are mainly the transitions among bands of Co 3d orbitals in nearly the same spin channel, which is reasonable since there is nearly nonspin flipping and sensitive to magnetization (see Fig. S7 in the Supplemental Material for more information [20]).

In the experimental data, below 100 K, besides InterB and InterC, we observed another absorption peak around 310 cm^{-1} [InterA in Fig. 1(c)]. However, this peak cannot be resolved in the calculated spectra [Fig. 3(f)]. This may

come from the overlapping of the low-energy peak with the overestimated Drude response. To pin down the origin of InterA, we established a tight-binding Hamiltonian from Wannier function and performed quite dense k sampling for integration of interband transitions. In the simulated $\sigma_1(\omega)$, a small absorption peak can be seen after SOC is considered, which is indicated by the red arrow in Fig. S4 of the Supplemental Material [20]. This peak is around 350 cm^{-1} , which is consistent with the position of InterA in Fig. 1(c). Checking the bands near the Fermi level, we notice that the SOC only triggers gaps along the nodal line [dashed circles in Fig. 3(a)] except for isolated Weyl points [Fig. S2(b)]. Thus, we ascribe the InterA to the interband transitions between the inverted bands, which are gapped by the SOC as marked by the red arrow in Fig. 3(c). These bands are very close to and compose of Weyl nodes.

In summary, we have carried out comprehensive optical and theoretical investigations on the electronic properties of a magnetic Weyl semimetal candidate $\text{Co}_3\text{Sn}_2\text{S}_2$. Experimental and theoretical results reveal a moderate electron correlation and show that the increasing exchange splitting renormalize the bands continuously, making the SOC-induced gap approaching the Fermi level. We have clearly identified the bands contributing to each absorption peak, including the magnetization sensitive and nonsensitive ones. The one from bands close to Weyl nodes is also identified. These results strongly suggest that the bands, including Weyl nodes, can be well controlled by magnetization, providing a useful way of tuning the topological properties in this magnetic Weyl semimetal for potential applications.

We thank Q. Niu, S. Q. Shen, Y. F. Xu, and Z. Y. Qiu for useful discussions. X. G. Q. acknowledges the support from NSFC (Projects No. 11974412 and No. 11774400) and MOST (Project No. 2017YFA0302903). H. M. W. acknowledges the support from the Ministry of Science and Technology of China under Grants No. 2016YFA0300600 and No. 2018YFA0305700, the National Science Foundation of China under Grants No. 11674369 and No. 11925408, the K. C. Wong Education Foundation (GJTD-2018-01), Beijing Municipal Science & Technology Commission (Z181100004218001), and Beijing Natural Science Foundation (Z180008). Y. M. D. acknowledges the support from NSFC (Project No. 11874206).

*These authors contributed equally to this work.

[†]hmweng@iphy.ac.cn

[‡]xgqiu@iphy.ac.cn

[1] E. Liu *et al.*, *Nat. Phys.* **14**, 1125 (2018).

[2] Q. Wang, Y. Xu, R. Lou, Z. Liu, M. Li, Y. Huang, D. Shen, H. Weng, S. Wang, and H. Lei, *Nat. Commun.* **9**, 3681 (2018).

- [3] Q. Xu, E. Liu, W. Shi, L. Muechler, J. Gayles, C. Felser, and Y. Sun, *Phys. Rev. B* **97**, 235416 (2018).
- [4] N. Morali, R. Batabyal, P. K. Nag, E. Liu, Q. Xu, Y. Sun, B. Yan, C. Felser, N. Avraham, and H. Beidenkopf, *Science* **365**, 1286 (2019).
- [5] D. F. Liu, A. J. Liang, E. K. Liu, Q. N. Xu, Y. W. Li, C. Chen, D. Pei, W. J. Shi, S. K. Mo, P. Dudin, T. Kim, C. Cacho, G. Li, Y. Sun, L. X. Yang, Z. K. Liu, S. S. P. Parkin, C. Felser, and Y. L. Chen, *Science* **365**, 1282 (2019).
- [6] R. Yu, W. Zhang, H.-J. Zhang, S.-C. Zhang, X. Dai, and Z. Fang, *Science* **329**, 61 (2010).
- [7] H. Weng, R. Yu, X. Hu, X. Dai, and Z. Fang, *Adv. Phys.* **64**, 227 (2015).
- [8] L. Muechler, E. Liu, Q. Xu, C. Felser, and Y. Sun, *arXiv:1712.08115*.
- [9] G. Xu, H. Weng, Z. Wang, X. Dai, and Z. Fang, *Phys. Rev. Lett.* **107**, 186806 (2011).
- [10] X. Wan, A. M. Turner, A. Vishwanath, and S. Y. Savrasov, *Phys. Rev. B* **83**, 205101 (2011).
- [11] C.-L. Zhang *et al.*, *Nat. Phys.* **13**, 979 (2017).
- [12] N. Nagaosa, J. Sinova, S. Onoda, A. H. MacDonald, and N. P. Ong, *Rev. Mod. Phys.* **82**, 1539 (2010).
- [13] D. Xiao, M.-C. Chang, and Q. Niu, *Rev. Mod. Phys.* **82**, 1959 (2010).
- [14] D. Yue and X. Jin, *J. Phys. Soc. Jpn.* **86**, 011006 (2017).
- [15] J. F. Steiner, A. V. Andreev, and D. A. Pesin, *Phys. Rev. Lett.* **119**, 036601 (2017).
- [16] Z. Fang, N. Nagaosa, K. S. Takahashi, A. Asamitsu, R. Mathieu, T. Ogasawara, H. Yamada, M. Kawasaki, Y. Tokura, and K. Terakura, *Science* **302**, 92 (2003).
- [17] B. Xu, Y. M. Dai, L. X. Zhao, K. Wang, R. Yang, W. Zhang, J. Y. Liu, H. Xiao, G. F. Chen, A. J. Taylor, D. A. Yarotski, R. P. Prasankumar, and X. G. Qiu, *Phys. Rev. B* **93**, 121110 (R) (2016).
- [18] Y. Shao, Z. Sun, Y. Wang, C. Xu, R. Sankar, A. J. Breindel, C. Cao, M. M. Fogler, A. J. Millis, F. Chou, Z. Li, T. Timusk, M. B. Maple, and D. N. Basov, *Proc. Natl. Acad. Sci. U.S.A.* **116**, 1168 (2019).
- [19] N. P. Armitage, E. J. Mele, and A. Vishwanath, *Rev. Mod. Phys.* **90**, 015001 (2018).
- [20] See Supplemental Material at <http://link.aps.org/supplemental/10.1103/PhysRevLett.124.077403> for further details of the sample characterizations and experimental techniques as well as for complementary data and analysis, which includes Refs. [21–31].
- [21] W. Schnelle, A. Leithe-Jasper, H. Rosner, F. M. Schappacher, R. Pöttgen, F. Pielnhofer, and R. Wehrich, *Phys. Rev. B* **88**, 144404 (2013).
- [22] C. C. Homes, M. Reedyk, D. A. Cradles, and T. Timusk, *Appl. Opt.* **32**, 2976 (1993).
- [23] G. Kresse and J. Furthmüller, *Phys. Rev. B* **54**, 11169 (1996).
- [24] J. P. Perdew, K. Burke, and M. Ernzerhof, *Phys. Rev. Lett.* **77**, 3865 (1996).
- [25] A. A. Mostofi, J. R. Yates, G. Pizzi, Y.-S. Lee, I. Souza, D. Vanderbilt, and N. Marzari, *Comput. Phys. Commun.* **185**, 2309 (2014).
- [26] Q. Wu, S. Zhang, H.-F. Song, M. Troyer, and A. A. Soluyanov, *Comput. Phys. Commun.* **224**, 405 (2018).
- [27] P. Blaha, K. Schwarz, P. Sorantin, and S. Trickey, *Comput. Phys. Commun.* **59**, 399 (1990).

- [28] R. Y. Chen, S. J. Zhang, J. A. Schneeloch, C. Zhang, Q. Li, G. D. Gu, and N. L. Wang, *Phys. Rev. B* **92**, 075107 (2015).
- [29] C. J. Tabert, J. P. Carbotte, and E. J. Nicol, *Phys. Rev. B* **93**, 085426 (2016).
- [30] D. Neubauer, J. P. Carbotte, A. A. Nateprov, A. Löhle, M. Dressel, and A. V. Pronin, *Phys. Rev. B* **93**, 121202(R) (2016).
- [31] Z.-G. Chen, R. Y. Chen, R. D. Zhong, J. Schneeloch, C. Zhang, Y. Huang, F. Qu, R. Yu, Q. Li, G. D. Gu, and N. L. Wang, *Proc. Natl. Acad. Sci. U.S.A.* **114**, 816 (2017).
- [32] M. Dressel and G. Gruner, *Electrodynamics of Solids* (Cambridge University Press, Cambridge, England, 2002).
- [33] L. J. Sandilands, W. Kyung, S. Y. Kim, J. Son, J. Kwon, T. D. Kang, Y. Yoshida, S. J. Moon, C. Kim, and T. W. Noh, *Phys. Rev. Lett.* **119**, 267402 (2017).
- [34] R. Yang, Z. Yin, Y. Wang, Y. Dai, H. Miao, B. Xu, X. Qiu, and C. C. Homes, *Phys. Rev. B* **96**, 201108(R) (2017).
- [35] D. Basov and T. Timusk, *Rev. Mod. Phys.* **77**, 721 (2005).
- [36] Y. M. Dai, A. Akrap, S. L. Bud'ko, P. C. Canfield, and C. C. Homes, *Phys. Rev. B* **94**, 195142 (2016).
- [37] W. Z. Hu, J. Dong, G. Li, Z. Li, P. Zheng, G. F. Chen, J. L. Luo, and N. L. Wang, *Phys. Rev. Lett.* **101**, 257005 (2008).
- [38] R. Yang, C. Le, L. Zhang, B. Xu, W. Zhang, K. Nadeem, H. Xiao, J. Hu, and X. Qiu, *Phys. Rev. B* **91**, 224507 (2015).
- [39] B. Xu, L. X. Zhao, P. Marsik, E. Sheveleva, F. Lyzwa, Y. M. Dai, G. F. Chen, X. G. Qiu, and C. Bernhard, *Phys. Rev. Lett.* **121**, 187401 (2018).
- [40] T. Timusk, J. P. Carbotte, C. C. Homes, D. N. Basov, and S. G. Sharapov, *Phys. Rev. B* **87**, 235121 (2013).
- [41] A. A. Burkov and L. Balents, *Phys. Rev. Lett.* **107**, 127205 (2011).
- [42] After checking the peak positions of InterA, B, and C, we find that the ratio between theoretical and experimental results are $E_{\text{theory}}^{\text{InterA}}/E_{\text{Exp}}^{\text{InterA}} = 1.12$, $E_{\text{theory}}^{\text{InterB}}/E_{\text{Exp}}^{\text{InterB}} = 1.69$, and $E_{\text{theory}}^{\text{InterC}}/E_{\text{Exp}}^{\text{InterC}} = 1.33$. We use the scaling factor of 1.33 to scale the measured $\sigma_1(\omega)$ below the energy of InterC for a qualitative comparison.
- [43] M. M. Qazilbash, J. J. Hamlin, R. E. Baumbach, L. Zhang, D. J. Singh, M. B. Maple, and D. N. Basov, *Nat. Phys.* **5**, 647 (2009).
- [44] G. Zhang, E. Gorelov, E. Sarvestani, and E. Pavarini, *Phys. Rev. Lett.* **116**, 106402 (2016).